

# An Efficient Convex Hull-based Vehicle Pose Estimation Method for 3D LiDAR

Ningning Ding<sup>1</sup>, Ruihao Ming<sup>1</sup>, Bo Wang<sup>1</sup>

**Abstract**—Vehicle pose estimation with LiDAR is essential in the perception technology of autonomous driving. However, due to incomplete observation measurements and sparsity of the LiDAR point cloud, it is challenging to achieve satisfactory pose extraction based on 3D LiDAR by using the existing pose estimation methods. In addition, the requirement for real-time performance further increases the difficulty of the pose estimation task. In this paper, we proposed a novel convex hull-based vehicle pose estimation method. The extracted 3D cluster is reduced to the convex hull, reducing the computation burden and retaining contour information. Then a novel criterion based on the minimum occlusion area is developed for the search-based algorithm, which can achieve accurate pose estimation. This criterion also makes the proposed algorithm especially suitable for obstacle avoidance. The proposed algorithm is validated on the KITTI dataset and a manually labeled dataset acquired at an industrial park. The results show that our proposed method can achieve better accuracy than the state-of-the-art pose estimation method while maintaining real-time speed.

## I. INTRODUCTION

Autonomous driving has drastically developed in the last decades. The safety of autonomous driving requires a reliable perception system to perceive surroundings for mobile platforms. In perception technology, 3D object detection is one of its main research directions, and numerous researchers have applied various 3D object detection [4], [5], [6], [7]. In particular, a 3D light detection and ranging (LiDAR) sensor has been extensively deployed to allow for centimeter-level accuracy, all-weather operation, and its ability to measure great distances compared with stereo cameras [8]. In this article, we specifically focus on 3D object detection based on LiDAR. 3D object detection based on LiDAR falls into two categories: traditional methods and deep learning methods. In recent years, various learning-based 3D object detection methods have been proposed, including VoxelNet [9], PointRCNN [10], PointPillars [11], CenterPoint [12], among others. Most of these approaches provide an end-to-end solution to 3D object detection based on a 3D convolutional neural network and exhibit outstanding performance. However, there are two inherent potential limitations. First, learning-based methods require labeling by humans, which is both severely laborious and time-consuming. Second, the performance of learning-based 3D object detection methods can be degraded when implemented in scenes different from

<sup>1</sup>Ningning Ding, Ruihao Ming, and Bo Wang are with Jiangsu Jingling Institute of Intelligent Manufacturing Co., Ltd., China. E-mail addresses: dingnn@mail.ustc.edu.cn

the training dataset or sensor configurations. On the contrary, the adaptability of traditional methods is much better. In the traditional 3D object detection pipeline of 3D LiDAR, it is generally necessary to first perform ground segmentation with the original 3D point cloud and then perform point cloud clustering with the non-ground point cloud. The 3D object detection task is finally completed after estimating the object's bounding box according to the clustering results. The main advantage of the traditional methods is that they do not need prior information about the environment for training. Thus, the generalization performance of the traditional method is better than the learning-based method.

The work in this paper focuses on estimating the vehicle's pose with the clustering point cloud in a LiDAR perception pipeline described above. The main contributions of this paper are listed as follows:

- We developed a convex hull-based vehicle pose estimation method for 3D LiDAR, a novel criterion based on the minimum occlusion area is employed, which can achieve better performance while maintaining real-time speed. Besides, the proposed method is especially suitable for path planning due to the minimum occlusion area criterion.
- Our proposed algorithm was evaluated with the KITTI dataset [16] and our own dataset. Experimental evidence corroborates the proposed algorithm exhibits promising performance compared with state-of-the-art methods.

## II. RELATED WORK

The current vehicle pose estimation algorithms for 3D LiDAR based on traditional methods can be categorized into two types: pose estimation algorithms based on specific point cloud distribution shapes and global pose estimation algorithms. The pose estimation algorithms based on the point cloud distribution shapes are generally classified into L-shape, U-shape, and E-shape [18], [19]. Since the L-shape has appeared most often in the distribution of 3D LiDAR point clouds [14], many methods have used this feature to estimate the pose of objects. Zhang et al. [13] proposed a search-based method for pose estimation of the vehicle. It iterates all possible directions of the rectangle, and multiple criteria are applied to evaluate the optimal fitting directions. However, this method is computationally expensive, and is hard to achieve real-time speed when using complex criteria such as the variance criterion. Kim et al. [23] proposed an iterative end-point fitting method to extract L-shape features from a 3D point cloud. This method starts with the minimum

and maximum clustering angle points as the end points of the baseline. The point that has the longest distance from the baseline to each point of the cluster is determined as the break-point. The final pose estimation bounding box was determined by extracting the farthest point from the baseline as the L-shaped corner point. However, this method assumes that all point clouds present a complete L-shape. To overcome this limitation, Zhao *et al.* [14] proposed a new corner edge-based L-shape fitting method. After calculating the approximate corner point, it was further judged whether the point was the corner point of the L-shape or the side point of the vehicle. Then the RANSAC algorithm was used to fit the L-shape features to obtain the pose estimation result.

Compared to the pose estimation method based on some specific shape, a global-based pose estimation algorithm depends less on the point cloud's specific geometry and focuses more on the global applicability of the algorithm. In reference [20], the authors proposed an orientation-corrected bounding box fitting method based on the convex hull and a line creation heuristic. With the help of the rapidity features of convex hull extraction, this algorithm can efficiently perform correct pose estimation even when the point cloud is sparse. An *et al.* [21] proposed a vehicle pose estimation algorithm using a low-end 3D LiDAR. This algorithm first established four vehicle models with different observation angles, then modeled the vehicle's measured size as a uniformly distributed sample, and finally applied the idea of template matching to estimate the vehicle's pose. Yang *et al.* [22] proposed a new vehicle pose estimation method based on edge distance. The introduced edge distance describes the distribution of the point clouds well. Then the bounding rectangle based on the edge distance is used to estimate the vehicle's pose. Meanwhile, if the vehicle has only one visible side or the point clouds are sparse, the correction is used to modify the bounding rectangle to obtain a more accurate vehicle pose estimation. He *et al.* [3] proposed a pose estimation method of moving vehicles based on the heuristic rules. It uses the edge length and edge visibility to heuristically screen the candidate orientations established by the convex hull sampling method. Then tracking heuristics are employed to smooth orientation estimation results. Liu *et al.* [2] presented a pose estimation method based on the convex-hull model and position inference. The bounding box's orientation is determined by multiple evaluation criteria. Sun *et al.* [1] present a dynamic vehicle pose estimation method with heuristic L-shape fitting and grid-based particle filter. A geometric shape classifier module divides clusters into symmetrical and asymmetrical ones. Then, a contour-based heuristic L-shape fitting module is introduced for asymmetrical clusters, and a structure-aware grid-based particle filter is used to estimate the pose of symmetrical clusters.

### III. METHODOLOGY

The proposed method consists of several steps to evaluate a candidate orientation for the vehicle, including convex

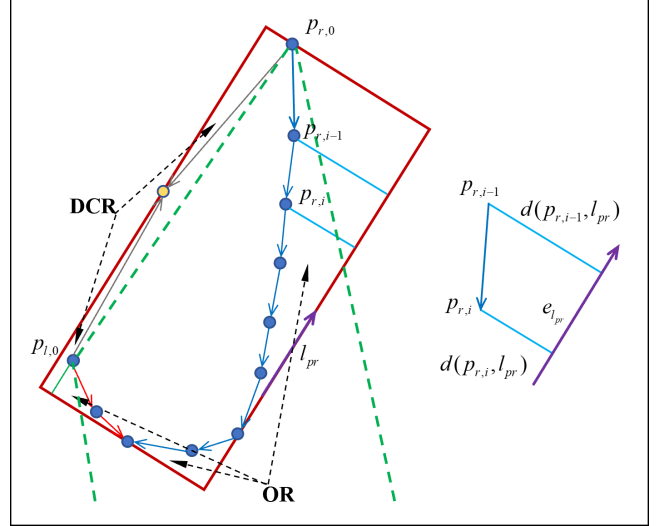


Fig. 1: Schematic illustration for calculating occlusion region's area.

hull extraction and score calculation. In this section, we will discuss the detailed implementation of the proposed algorithm, as well as its fundamentals.

---

#### Algorithm 1 Pipeline of the Proposed Algorithm

---

```

Input : cluser's point cloud cluster_pc
Output: orientation estimation value  $\theta^*$ 
occluAreaArray  $\leftarrow$  an empty vector;
cluster_pc_2d  $\leftarrow$  projection2D(cluster_pc)
ch_pts  $\leftarrow$  convexHull(cluster_pc_2d)
for i in  $[0, \text{ch\_pts.size}())$  do
| pt_azimuth.push_back(atan2(ch_pts[i].y, ch_pts[i].x));
end
vl_idx_l = argmini(pt_azimuth[i]);
vl_idx_r = argmaxi(pt_azimuth[i]);
for  $\theta$  in  $[0, \pi/2]$  step  $\delta$  do
| for i in  $[0, 4)$  do
| |  $\vec{e}_1 \leftarrow [\cos\theta, \sin\theta]$ ,  $\vec{e}_2 \leftarrow [-\sin\theta, \cos\theta]$ ;
| |  $C_1 \leftarrow P_t \cdot \vec{e}_1$ ,  $C_2 \leftarrow P_t \cdot \vec{e}_2$ ;
| | line[0].a  $\leftarrow \cos\theta$ , line[0].b  $\leftarrow \sin\theta$ , line[0].c  $\leftarrow \min\{C_1\}$ ;
| | line[1].a  $\leftarrow -\sin\theta$ , line[1].b  $\leftarrow \cos\theta$ , line[1].c  $\leftarrow \min\{C_2\}$ ;
| | line[2].a  $\leftarrow \cos\theta$ , line[2].b  $\leftarrow \sin\theta$ , line[2].c  $\leftarrow \max\{C_1\}$ ;
| | line[3].a  $\leftarrow -\sin\theta$ , line[3].b  $\leftarrow \cos\theta$ , line[3].c  $\leftarrow \max\{C_2\}$ ;
| end
| [projL_idx_l, projL_idx_r] = DetectVisibleEdge();
| [ $\theta$ , occluArea] = CalculateOcclusionArea();
| occluAreaArray.push_back( $[\theta, \text{occluArea}]$ )
end
 $\theta^* = \text{occluAreaArray}[\text{argmin}_i(\text{occluAreaArray}[i].\text{occluArea})].\theta$ ;

```

---

Since we only care about the yaw angle of objects in the autonomous driver application, we can project the 3D point cloud onto the x-y plane. This reduces the original clusters from 3D space to 2D space and reduces the computational burden for the following steps. However, the projected 2D cluster lost the information along the z-axis. To get the height and position of the bounding box along the z-axis, we should calculate the minimum and maximum z values of the 3D cluster, namely  $z_{\min}$  and  $z_{\max}$ , before projection. The height of the bounding box equals  $z_{\max} - z_{\min}$ , and the position of the bounding box along the z-axis is  $(z_{\max} - z_{\min})/2$ . The aim of

this work is to improve speed while ensuring pose estimation accuracy. So we choose to exact the contour from the cluster and avoid dealing with point clouds directly. To this end, we can extract the convex-hull points from the projected 2D cluster. For consideration of both simplicity and efficiency, we choose the Graham scan method [15] to generate a set of convex-hull points from the projected 2D point cloud.

Then, we use a search-based algorithm to find the optimal vehicle pose. The key issue of this algorithm is to choose the proper criterion to decide which orientation is the best option. There are already many criteria proposed in the literature, like area minimization, closeness maximization, and variance minimization [13]. However, these criteria are only appropriate for the 2D cluster, and its performance will degrade when using a convex hull. This is due to some information being lost when reducing the 2D cluster into a convex hull. Besides, these criteria are mainly suitable when the cluster is an L-shape. However, due to occlusion and different viewing angles, the L-shape cannot be observed in some cases.

In this paper, we proposed a novel criterion based on the minimum occlusion area or maximum driveable area. This is a straightforward idea since the wrong estimation of vehicle orientation will result in the driveable region being occupied by mistake. The goal of our criterion is to minimize this wrong occlusion region (OR), as presented in Figure 1. It should be noted that the area of OR is hard to calculate if using the original 2D cluster. Fortunately, this becomes easy after converting the 2D cluster to a convex hull. The pipeline of the proposed algorithm is presented in Alg.1.

#### A. Visible edge selection

Inspired by the concept of calculus, the area of OR can be divided into many trapezoids, as shown in Figure 1. To calculate its area, the first thing is to choose the appropriate projection edge from the rectangle's four edges so that we can calculate the trapezoid's height.

Considering the vehicle body facing away from the LiDAR can't be detected, the rectangle's edges here have no valid information to decide the vehicle's pose. Therefore, we choose the visible edges as the projection line. Firstly, we calculate the two boundary points of convex hull points according to the azimuth angle. Then we connect the two border points with the LiDAR origin to form a valid region as shown in the green triangle in Figure 1. Only points and edges in this region will be considered for vehicle pose estimation. The edge contacts with border lines first will be selected as the projection edge. We first calculate the intersection of border lines and rectangle edges. If the intersection is on the rectangular edge, this edge is chosen as the candidate projection edge. If the intersection coincides with a rectangular vertice, two adjacent rectangular edges will be chosen as the candidate projection edge. Then in all the candidate edges, the one whose intersection is closest to the LiDAR is the projection edge. If the closest intersection happens to be the rectangular vertice, the edge located in the

valid region will be the projection edge. The detail of this process is presented in Alg. 2.

---

#### Algorithm 2 Visible Edge Selection

---

**Input** : Rectangle edges, vertexes, and boundary lines  
**Output**: Projection edges index

```

candi_pL_idx ← an empty vector;
candiIdx_array ← an empty vector;
projL_idx_l = SelectProjLine(vl_idx_l, line_vl_l);
projL_idx_r = SelectProjLine(vl_idx_r, line_vl_r);
Procedure SelectProjLine(vl_idx, line_vl)
    for i in [0,4) do
        if (is_vertex_ and i == {recv_idx_ or recv_idx_ + 1}) then
            | continue;
        end
        vl_poi = calcuIntersection(line[i], line_vl_);
        vl2rec_di_l = dst(vl_poi, rcr_pts[idx_l]);
        vl2rec_di_r = dst(vl_poi, rcr_pts[idx_r - 1]);
        edge_len = dst(rcr_pts[idx_r - 1], rcr_pts[idx_l]);
        if (max(vl2rec_di_l, vl2rec_di_r) < edge_len) then
            | candi_pL_idx.push_back(idx_l);
        end
        if (not is_recv_) then
            | dst_i = abs(max(vl2rec_di_l, vl2rec_di_r) - edge_len);
            | candiIdx_array[idx_].idx_ = idx_;
            | candiIdx_array[idx_].dst_ = dst_i;
        end
    end
    sort(candiIdx_array);
    if (not is_recv_ and candi_pL_idx.empty()) then
        candi_pL_idx.push_back(candiIdx_array[0].idx_);
        candi_pL_idx.push_back(candiIdx_array[1].idx_);
        is_recv_ = true;
        recv_idx_ = min(candiIdx_array[0].idx_, candiIdx_array[1].idx_);
    end
    for i in [0, candi_pL_idx.size()) do
        can_vl_poi = calcuIntersection(line[candi_pL_idx[i]], line_vl_);
        len_can_vl_poi.push_back(len(can_vl_poi));
    end
    if (is_recv_ and len(rcr_pts[recv_idx_]) < min{len_can_vl_poi}) then
        if isVisible(rcr_pts[recv_idx_]) then
            | projL_idx_ = recv_idx_;
        else
            | projL_idx_ = recv_idx_ + 1;
        end
    else
        | projL_idx_ = argmax_i(len_can_vl_poi[i]);
    end
    return projL_idx_
```

---

#### B. Calculate the Occlusion Area

After determining the projection edge, we can calculate the trapezoid's height and further get the whole OR's area. We start from the right boundary point. There are two different directions to search for the next point. The adjacent point in the visible region will be selected as the next point. We will continue to search the rest of the points in this direction, as shown in Figure 1. The two adjacent points along the right projection edge form a trapezoid. For the i-th trapezoid, its area can be calculated as

$$OR_{r,i} = [d(p_{r,i}, l_{pr}) + d(p_{r,i-1}, l_{pr})] \cdot (\overrightarrow{p_{r,i}p_{r,i-1}} \cdot \overrightarrow{e_{l_{pr}}}) / 2 \quad (1)$$

where  $d(p_{r,i}, l_{pr})$  denotes the relative distance of  $p_{r,i}$  to the projection line  $l_{pr}$ ,  $\overrightarrow{e_{l_{pr}}}$  is the unit direction vector of projection line  $l_{pr}$ .

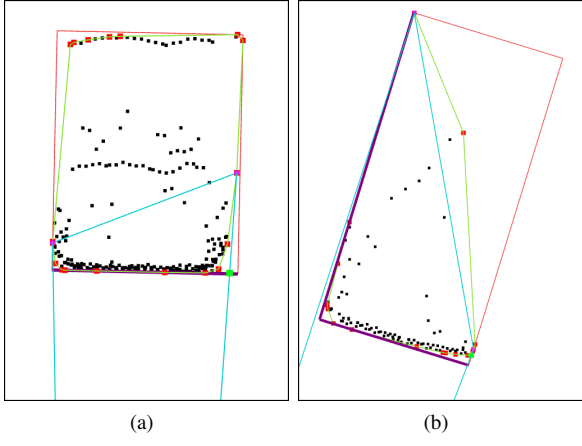


Fig. 2: Illustration of the projection line selection (the purple line denotes the projection edge)

### Algorithm 3 Occlusion Area Calculation

**Input** : Projection edge index

**Output**: Area of the occlusion region

```

iter_dir_l ← 1; iter_dir_r ← 1;
if vl_idx_l + 1 == vl_idx_r or isVisible(ch_pts[vl_idx_l - 1]) then
| iter_dir_l = -1;
end
if vl_idx_r + 1 == vl_idx_l or isVisible(ch_pts[vl_idx_r - 1]) then
| iter_dir_r = -1;
end
[occusion_area_r, gap_num_r] = CalculateOR(projL_idx_r, vl_idx_r,
vl_idx_l, ch_pts.size);
[occusion_area_l, gap_num_l] = CalculateOR(projL_idx_l, vl_idx_l,
vl_idx_r, gap_num_r);
occusion_area = occusion_area_l + occusion_area_r;

Procedure CalculateOR(projL_idx_-, vl_idx_-, vl_idx_n, iter_dir_-, iter_num_)
occusion_area_ ← 0;
gap_num_ ← 0;
idx ← vl_idx_--;
for iter_num in [0, iter_max] do
| line_vector = [line[projL_idx_].b, -line[projL_idx_].a];
| pt_c = [ch_pts[idx].x, ch_pts[idx].y];
| pt_n = [ch_pts[idx + iter_dir_].x, ch_pts[idx + iter_dir_].y];
| ch_lineseg = pt_n - pt_c;
| trapezoid_h = ch_lineseg · line_vector;
| idx_last_ = idx;
| if idx ≠ vl_idx_n and trapezoid_h · break_condition < 0 then
| | break;
| end
| if idx == vl_idx_n then
| | break;
| end
| trapezoid_u = pt2linedst(pt_c, line[projL_idx_]);
| trapezoid_l = pt2linedst(pt_n, line[projL_idx_]);
| trapezoid_area = (trapezoid_u + trapezoid_l) · trapezoid_h / 2;
| occusion_area_+ = trapezoid_area;
| break_condition = trapezoid_h;
| idx+ = iter_dir_;
| end
while idx_last_ ≠ vl_idx_n do
| | idx_last_+ = iter_dir_;
| | gap_num_++;
| end
return [occusion_area_, gap_num_]
end

```

To ensure the trapezoid is in the visible region, we should give a stopping criterion to judge whether the calculated

trapezoid is valid and stop the next calculation. We first calculate the projection of  $\vec{p_{r,i-1}p_{r,i}}$  and  $\vec{p_{r,i-2}p_{r,i-1}}$  on projection edge  $l_{pr}$ . If the two projection vector is in the opposite direction, it means that the current trapezoid is not valid, and the next calculation is terminated. This stopping criterion can be simplified by calculating the product of  $\vec{p_{r,i-1}p_{r,i}} \cdot \vec{e_{l_{pr}}}$  and  $\vec{p_{r,i-2}p_{r,i-1}} \cdot \vec{e_{l_{pr}}}$ . If the sign of this product is negative, the stopping criterion is activated. If the last valid point happens to be the left boundary point, it means the occlusion area calculation has been completed. If the last valid point is not the left boundary point, we need to search for the valid trapezoid from the left boundary point until it reaches the breakpoint. Finally, we can get the area of the occlusion region when the fitted rectangle is in a certain direction. The detail of this process is presented in Alg. 3. It should be noted that the fitted rectangle's possible direction  $\theta$  ranges from  $0^\circ$  to  $90^\circ$ , as the two consecutive sides of a rectangle are orthogonal and we only care about the single edge that falls between  $0^\circ$  and  $90^\circ$ . Thus, we can traverse the possible direction of the rectangle with a fixed resolution. Then we calculate the corresponding occlusion region's area and choose the orientation with the minimum occlusion area as the estimated orientation of our algorithm. Once we determine the rectangle's orientation, its four edges can be calculated easily, and the detail can be found in reference [13]. Combing the bounding box's position and dimension along the z-axis, we can finally get the 3D bounding box for an object using our algorithm.

## IV. EXPERIMENTS

To evaluate the correctness and efficiency of our proposed algorithm, experiments are carried out on the KITTI dataset and a manually labeled dataset. We compare the proposed algorithm with state-of-the-art vehicle pose estimation methods like RANSAC L-shape fitting method [14] and convex hull heuristic (CHH) method [3]. Since our method has not associated with any tracking algorithm, the vanilla CHH without tracking is used here for a fair comparison. These algorithms were all implemented in C++, and there was no parallelization or GPU acceleration enabled. We used a desktop equipped with an AMD Ryzen™ 9 5900X processor to execute these algorithms.

In order to exclude the influence of ground segmentation and clustering, we used the labeled information to extract the point cloud for every single object directly. Since we mainly focus on vehicle pose estimation, pedestrians and other non-vehicle objects in the KITTI dataset will not participate in the evaluation. Then the vehicle pose estimation algorithm will read the single object's point cloud and calculate its orientation. It is worth noting that the orientation value in KITTI labels ranges from  $-\pi$  to  $\pi$ . We convert it to the range of 0 to  $\pi/2$  to be consistent with our algorithm. After comparing the estimated value with the ground truth information, we can evaluate the pose estimation performance.

We employed widely used evaluation metrics, including orientation error and absolute orientation error, to evaluate

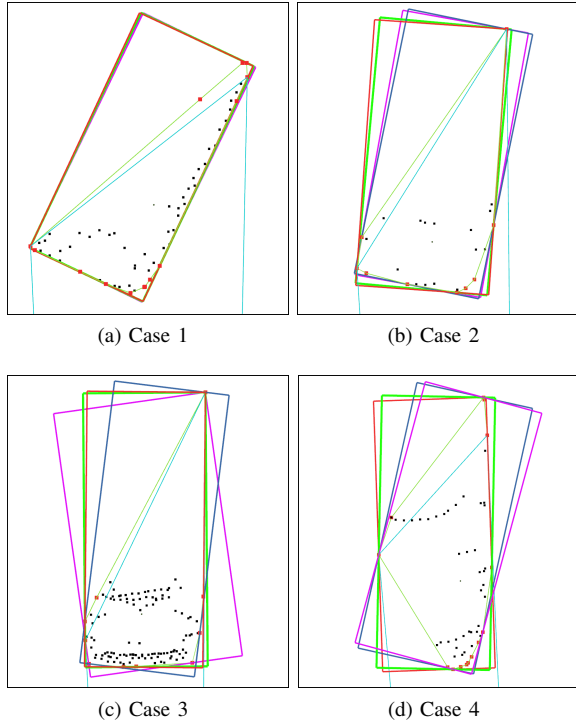


Fig. 3: Sample results of vehicle pose estimation on KITTI dataset. Green boxes from the ground truth, purple boxes come from the RANSAC L-shape fitting method, blue boxes come from the CHH method, and red boxes from the proposed algorithm.

the accuracy of vehicle pose estimation. The absolute orientation error reflects the estimation bias without considering its direction. Furthermore, the running time was also measured to verify that our method is computationally efficient.

#### A. KITTI Dataset

The KITTI Dataset consists of 7481 training images and 7518 test images as well as the corresponding point clouds. The point clouds were collected by a Velodyne HDL-64E rotating 3D LiDAR. A total of 26824 objects in the KITTI dataset will be evaluated.

The mean and standard deviation of orientation error and absolute orientation error are listed in Table I. The RANSAC L-shape method gets the worst result, especially in the STD item. This shows that this method is not very stable. The CHH method has a few improvements over the RANSAC L-shape method. Compared with the CHH method, the proposed algorithm improves the mean absolute orientation error by 48.6% from  $3.3648^\circ$  to  $1.7299^\circ$ , which shows our method achieves significant improvement in vehicle pose estimation. Besides, our method also has a 40% improvement in STD items which proves our method is more robust. Table I also presents the computation time fitting one object. All three methods have good computation performance. The proposed method only spends an average of 0.2872 ms for one single object which can achieve real-time performance

even fitting 100 objects simultaneously. Figure 4 illustrates the distribution of absolute orientation error on the KITTI dataset. As shown in Figure 4, most errors are distributed from  $0^\circ$  to  $1^\circ$  with the proposed method. On the contrary, the other two methods have much fewer results from  $0^\circ$  to  $1^\circ$  and have more scattered distribution. These results suggest that the proposed method is more consistent and stable than other methods.

The examples of fitting results on the KITTI dataset are shown in Figure 3. In case 1, the cluster is L-shape which is very common in the KITTI dataset, and all three methods get a good fitting result. The cluster in case 2 is still an L-shape but very sparse. Only the proposed method achieves good fitting. In case 3, the cluster is occluded by the front of the vehicle. Our method achieves the best fitting result, and the other two methods exist large orientation estimation errors. The cluster in case 4 has occlusion. The proposed method can still get the right fitting result.

#### B. Own Dataset

Our own dataset is collected with a Velodyne Puck (VLP-16) 3D LiDAR in an industrial park, as shown in Figure 6. We labeled 600 frames of LiDAR point cloud using the 3D bounding box annotation tool: SUSTechPOINTS [17]. Then we convert these labels to the KITTI format. The rest procedures are the same as the KITTI dataset.

Table I presents the quantization results of pose estimation on our own dataset. Compared to the KITTI dataset, the mean and STD of orientation error drop a lot and the running time increased. This is because the objects we labeled are located at a relatively close distance. Therefore, the point cloud of the labeled objects is denser and less occluded. For the RANSAC L-shape fitting method, its pose estimation accuracy improves a lot, only slightly worse than our algorithm. However, its running time has almost tripled compared with the KITTI dataset which shows that this method is sensitive to the number of point clouds. The proposed algorithm still gets the best result on our own dataset except for the running time. Figure 5 presents the distribution of absolute orientation error on our own dataset. As shown in Figure 5, the proposed method and RANSAC L-shape fitting method have more concentrated distribution. Besides, there is a peak near  $4^\circ$  in the histogram of our method.

The examples of fitting results on our own dataset are shown in Figure 7. In case 1, the cluster is L-shape which is also common in our own dataset, and our method gets the best fitting result. The cluster in case 2 exists occlusion, the CHH method gets the wrong orientation estimation and the other two methods get the good fitting. In case 3, there exist a rear-view mirror on the side of the vehicle which can be seen often in our data sets. Only the RANSAC L-shape fitting method achieves good fitting. This shows our method and CHH method are both sensitive to the protruding objects. This also explains the peak near  $4^\circ$  in the histogram of our method. In case 4, the vehicle is occluded by the front of the vehicle and there are only a few points on the side of

TABLE I: Orientation error and running time comparison between different fitting methods on KITTI dataset

Method	Absolute Error		Error		Running Time	
	Mean (deg) ↓	STD (deg) ↓	Mean (deg) ↓	STD (deg) ↓	Mean (ms) ↓	STD (ms) ↓
RANSAC L-shape	3.8034	7.2455	1.5586	8.0333	0.3612	0.6333
CHH	3.3648	6.5149	1.4815	7.1813	<b>0.2413</b>	<b>0.2056</b>
Proposed	<b>1.7299</b>	<b>3.8899</b>	<b>0.5075</b>	<b>4.2269</b>	0.2872	0.2124

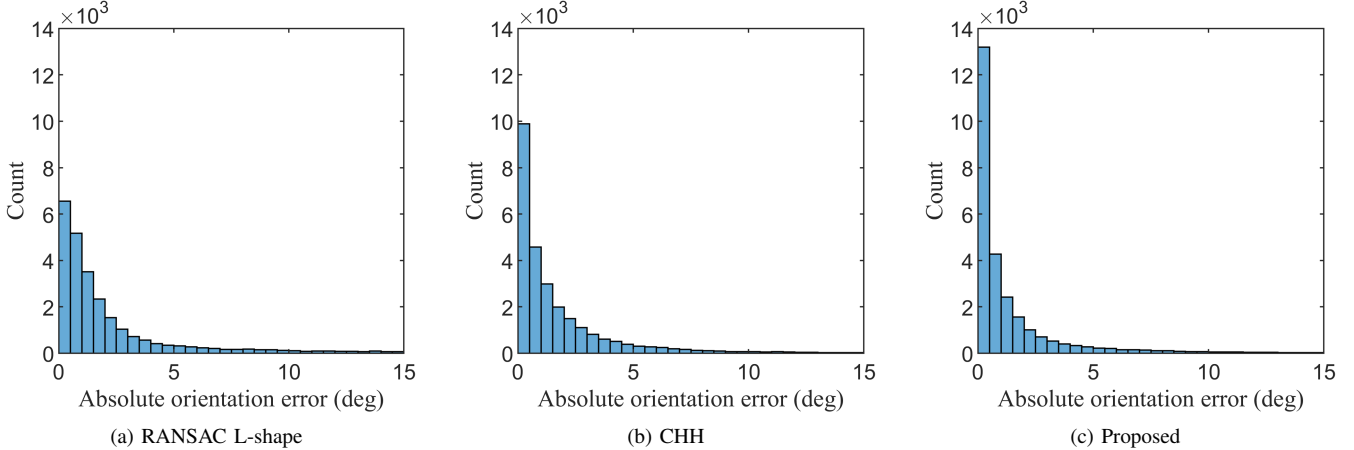


Fig. 4: Distribution of absolute orientation error on KITTI dataset

TABLE II: Orientation error and running time comparison between different fitting methods on our own dataset

Method	Absolute Error		Error		Running Time	
	Mean (deg) ↓	STD (deg) ↓	Mean (deg) ↓	STD (deg) ↓	Mean (ms) ↓	STD (ms) ↓
RANSAC L-shape	1.3325	3.6072	0.2441	3.8377	1.0656	1.0650
CHH	2.9992	5.6494	1.1150	6.2983	<b>0.3372</b>	<b>0.1295</b>
Proposed	<b>1.3101</b>	<b>2.2445</b>	<b>-0.0115</b>	<b>2.5989</b>	0.3763	0.1406

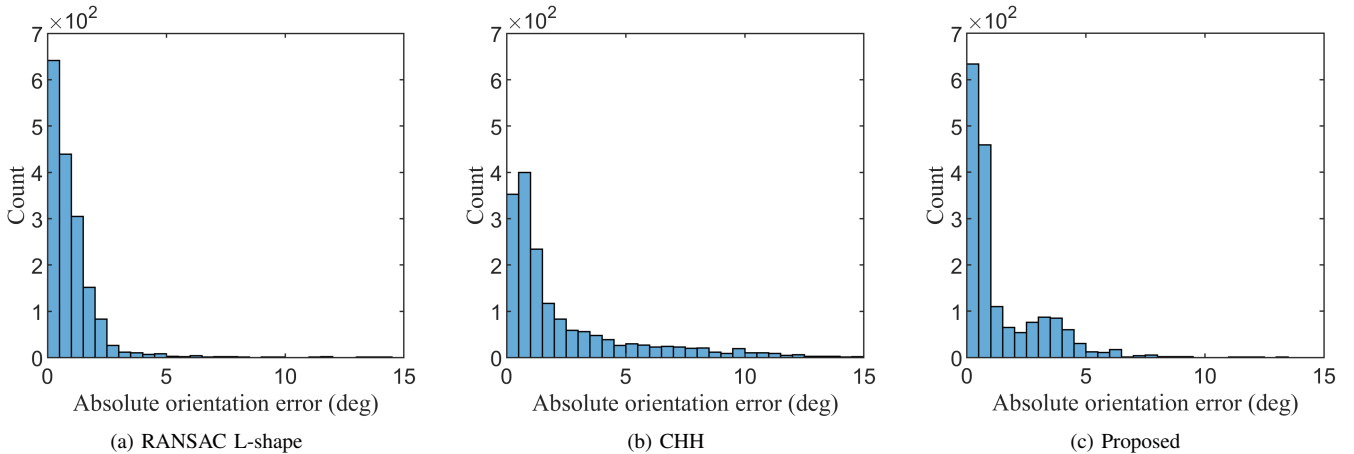


Fig. 5: Distribution of absolute orientation error on our own dataset.

the vehicle. The RANSAC L-shape fitting method gets the wrong fitting due to the cluster is curving. The other two methods achieve good fitting.

## V. CONCLUSION

A novel convex hull-based vehicle pose estimation method is proposed in this paper. The convex hull extraction and the novel criterion based on the minimum occlusion area make our algorithm achieve high pose estimation accuracy

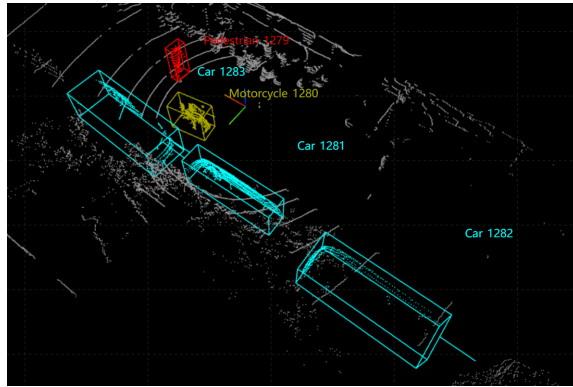


Fig. 6: A demonstration of our own dataset and its annotation.

while maintaining real-time speed. Experimental results on the KITTI dataset and a manually labeled dataset show that the proposed method can estimate the vehicle's pose accurately and stably while maintaining real-time speed. In our future work, we will incorporate our method with tracking algorithms to smooth the orientation estimation result and reduce unnecessary search. we also want introduce RANSAC in our method to improve the robustness to noise.

## REFERENCES

[1] J. Sun, Y.-M. Ji, and S.-D. Liu, "Dynamic vehicle pose estimation with heuristic l-shape fitting and grid-based particle filter," *Electronics*, vol. 12, no. 8, p. 1903, 2023.

[2] K. Liu and J. Wang, "Fast dynamic vehicle detection in road scenarios based on pose estimation with convex-hull model," *Sensors*, vol. 19, no. 14, p. 3136, 2019.

[3] Y. He, W. Zhang, and M. Yang, "Pose estimation of moving vehicles based on heuristic rules for autonomous driving," in *2022 IEEE International Conference on Robotics and Biomimetics (ROBIO)*, pp. 729–734, IEEE, 2022.

[4] Y. Li, Z. Ge, G. Yu, J. Yang, Z. Wang, Y. Shi, J. Sun, and Z. Li, "Bevdepth: Acquisition of reliable depth for multi-view 3d object detection," *arXiv preprint arXiv:2206.10092*, 2022.

[5] Y. Wang, B. Yang, R. Hu, M. Liang, and R. Urtasun, "Plumenet: Efficient 3d object detection from stereo images," in *2021 IEEE/RSJ International Conference on Intelligent Robots and Systems (IROS)*, pp. 3383–3390, IEEE, 2021.

[6] X. Ma, W. Ouyang, A. Simonelli, and E. Ricci, "3d object detection from images for autonomous driving: a survey," *arXiv preprint arXiv:2202.02980*, 2022.

[7] G. Zamanakos, L. Tsochatzidis, A. Amanatiadis, and I. Pratikakis, "A comprehensive survey of lidar-based 3d object detection methods with deep learning for autonomous driving," *Computers & Graphics*, vol. 99, pp. 153–181, 2021.

[8] J. Behley, M. Garbade, A. Milioto, J. Quenzel, S. Behnke, C. Stachniss, and J. Gall, "Semantickitti: A dataset for semantic scene understanding of lidar sequences," in *Proceedings of the IEEE/CVF International Conference on Computer Vision*, pp. 9297–9307, 2019.

[9] Y. Zhou and O. Tuzel, "Voxelnet: End-to-end learning for point cloud based 3d object detection," in *Proceedings of the IEEE conference on computer vision and pattern recognition*, pp. 4490–4499, 2018.

[10] S. Shi, X. Wang, and H. Li, "Pointrenn: 3d object proposal generation and detection from point cloud," in *Proceedings of the IEEE/CVF conference on computer vision and pattern recognition*, pp. 770–779, 2019.

[11] A. H. Lang, S. Vora, H. Caesar, L. Zhou, J. Yang, and O. Beijbom, "Pointpillars: Fast encoders for object detection from point clouds," in *Proceedings of the IEEE/CVF conference on computer vision and pattern recognition*, pp. 12697–12705, 2019.

[12] T. Yin, X. Zhou, and P. Krahenbuhl, "Center-based 3d object detection and tracking," in *Proceedings of the IEEE/CVF conference on computer vision and pattern recognition*, pp. 11784–11793, 2021.

[13] X. Zhang, W. Xu, C. Dong, and J. M. Dolan, "Efficient l-shape fitting for vehicle detection using laser scanners," in *2017 IEEE Intelligent Vehicles Symposium (IV)*, pp. 54–59, IEEE, 2017.

[14] C. Zhao, C. Fu, J. M. Dolan, and J. Wang, "L-shape fitting-based vehicle pose estimation and tracking using 3d-lidar," *IEEE Transactions on Intelligent Vehicles*, vol. 6, no. 4, pp. 787–798, 2021.

[15] R. L. Graham, "An efficient algorithm for determining the convex hull of a finite planar set," *Info. Pro. Lett.*, vol. 1, pp. 132–133, 1972.

[16] A. Geiger, P. Lenz, C. Stiller, and R. Urtasun, "Vision meets robotics: The kitti dataset," *The International Journal of Robotics Research*, vol. 32, no. 11, pp. 1231–1237, 2013.

[17] E. Li, S. Wang, C. Li, D. Li, X. Wu, and Q. Hao, "Sustech points: A portable 3d point cloud interactive annotation platform system," in *2020 IEEE Intelligent Vehicles Symposium (IV)*, pp. 1108–1115, IEEE, 2020.

[18] F. Xu, H. Liang, Z. Wang, L. Lin, and Z. Chu, "A real-time vehicle detection algorithm based on sparse point clouds and dempster-shafer fusion theory," in *2018 IEEE International Conference on Information and Automation (ICIA)*, pp. 597–602, IEEE, 2018.

[19] D. Wittmann, F. Chucholowski, and M. Lienkamp, "Improving lidar data evaluation for object detection and tracking using a priori knowledge and sensorfusion," in *2014 11th International Conference on Informatics in Control, Automation and Robotics (ICINCO)*, vol. 1, pp. 794–801, IEEE, 2014.

[20] B. Naujoks and H.-J. Wuensche, "An orientation corrected bounding box fit based on the convex hull under real time constraints," in *2018 IEEE Intelligent Vehicles Symposium (IV)*, pp. 1–6, IEEE, 2018.

[21] J. An and E. Kim, "Novel vehicle bounding box tracking using a low-end 3d laser scanner," *IEEE Transactions on Intelligent Transportation Systems*, vol. 22, no. 6, pp. 3403–3419, 2020.

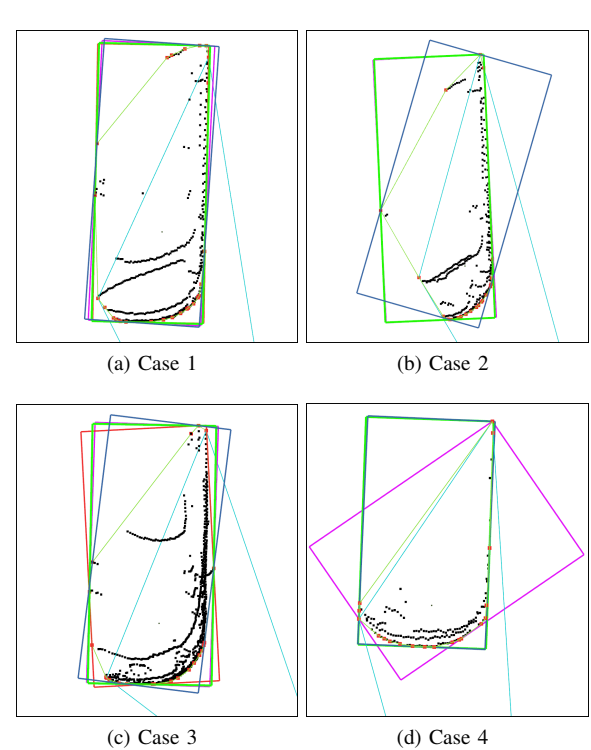


Fig. 7: Sample results of vehicle pose estimation on our own dataset. Green boxes from the ground truth, purple boxes come from the RANSAC L-shape fitting method, blue boxes come from the CHH method, and red boxes from the proposed algorithm.

- [22] J. Yang, G. Zeng, W. Wang, Y. Zuo, B. Yang, and Y. Zhang, “Vehicle pose estimation based on edge distance using lidar point clouds (poster),” in *2019 22th International Conference on Information Fusion (FUSION)*, pp. 1–6, IEEE, 2019.
- [23] D. Kim, K. Jo, M. Lee, and M. Sunwoo, “L-shape model switching-based precise motion tracking of moving vehicles using laser scanners,” *IEEE Transactions on Intelligent Transportation Systems*, vol. 19, no. 2, pp. 598–612, 2017.